01 Jan 2023

Effect Of Mechanical Activation On Carbothermal Synthesis And Densification Of ZrC

Nina Obradović

Lun Feng

Suzana Filipović

Miljana Mirković

et. al. For a complete list of authors, see https://scholarsmine.mst.edu/matsci_eng_facwork/3210

Recommended Citation

N. Obradović et al., "Effect Of Mechanical Activation On Carbothermal Synthesis And Densification Of ZrC," *Journal of the European Ceramic Society*, Elsevier, Jan 2023.
The definitive version is available at https://doi.org/10.1016/j.jeurceramsoc.2023.08.007

Journal of the European Ceramic Society xxx (xxxx) xxx

Contents lists available at ScienceDirect

Journal of the European Ceramic Society

journal homepage: www.elsevier.com/locate/jeurceramsoc

Effect of mechanical activation on carbothermal synthesis and densification of ZrC

Nina Obradović [a,b,*], Lun Feng [b,c], Suzana Filipović [a,b], Miljana Mirković [d], Darko Kosanović [a,b], Jelena Rogan [e], William G. Fahrenholtz [b]

[a] Institute of Technical Sciences of the Serbian Academy of Sciences and Arts, Knez Mihailova 35/IV, 11000 Belgrade, Serbia
[b] Department of Materials Science and Engineering, Missouri University of Science and Technology, Rolla, MO 65409, USA
[c] Blue Origin LLC, Kent, WA, USA
[d] University of Belgrade, "Vinča" Institute of Nuclear Sciences - National Institute of the Republic of Serbia, Department of Material Science, 11000 Belgrade, Serbia
[e] Department of General and Inorganic Chemistry, Faculty of Technology and Metallurgy, University of Belgrade, 11120 Belgrade, Serbia

ARTICLE INFO

Keywords:
ZrC
Mechanical activation
SEM
Mechanical properties
SPS

ABSTRACT

Zirconium carbide ceramics were prepared by carbothermal reduction of ZrO_2 and C that were mixed by high-energy ball milling. Powders were milled for times from 0 to 120 min in air. As milling time increased, the surface area of the powders increased, indicating significant particle size reduction. Milled powders were reacted at 1600 °C and then densified by spark plasma sintering at 2000 °C, which was sufficient to convert the starting powders to zirconium carbide. Unmilled powders did not reach full density. Milled powders reached full density, but ZrO_2 impurities were found for specimens prepared from powders milled for 60 and 120 min. Microstructure analysis showed that grain size was less than 2 μm for ceramics produced from powder milled for 15 min. Based on densification onset temperature and impurity levels, a milling time of 15 min gives the best balance of particle size reduction to promote densification while minimizing impurity levels.

1. Introduction

Zirconium carbide (ZrC) ceramics have been studied through the last two decades due to appealing properties that include extremely high melting point (~3500 °C), relatively low density (6.7 g/cm^3), moderate thermal conductivity (20.5 W·m^{-1}K^{-1} at 25 °C), good mechanical properties as well as excellent high-temperature stability. Like other carbides of the transition metals of Groups IV, V, and VI, ZrC exhibits an unusual combination of properties that are useful for refractory applications. ZrC has been one of the most promising candidates for structural applications that involve temperatures above 1800 °C [1–3]. Furthermore, ZrC is being considered as a structural and fission product barrier coating material for TRISO (tri-isotropic) coated nuclear fuel used in high temperature reactors (HTR's), replacing or in addition to the currently used silicon carbide (SiC) [4].

Several methods including the solid-state reaction of Zr and C, carbothermal reduction, and solution-based methods have been reported for the synthesis of ZrC powders [5–13]. Among them, owing to the simple processing, low production cost and high purity of the synthesized powder, the carbothermal reduction of ZrO_2 is the most common method for synthesizing ZrC powder [14]. Conventional carbothermal reduction using starting particles with sizes in the range from several microns to tens of microns in diameter can require temperatures above 1500 °C and reaction times of several hours for complete reaction, which results in a significant growth of the synthesized particles [7]. Likewise, conventional heating methods for densification can also lead to grain growth, which results in low relative densities. Spark plasma sintering (SPS) has a potential advantage because of heating and cooling rates on the order of hundreds of degrees per minute that can reduce total processing times from hours to just a few minutes [15]. The current that passed through the specimens during SPS was reported to increase the rate of compound formation and to decrease the incubation time for the nucleation of the new phases [16]. A few papers report using a combination of carbothermal reduction and SPS to obtain ZrC ceramics, but they did not reach full density due to grain growth that resulted in porosity trapped within the grains of the sintered specimens [14,17–20]. The key issue to produce dense ZrC ceramics, and most ceramics in general, is to control the grain growth/densification behaviour [21].

One of the possible ways to minimize grain growth during sintering is addition of very small quantities of various compounds and/or sintering

* Corresponding author at: Institute of Technical Sciences of the Serbian Academy of Sciences and Arts, Knez Mihailova 35/IV, 11000 Belgrade, Serbia.
E-mail address: nina.obradovic@itn.sanu.ac.rs (N. Obradović).

https://doi.org/10.1016/j.jeurceramsoc.2023.08.007
Received 8 March 2023; Received in revised form 4 August 2023; Accepted 7 August 2023
Available online 9 August 2023

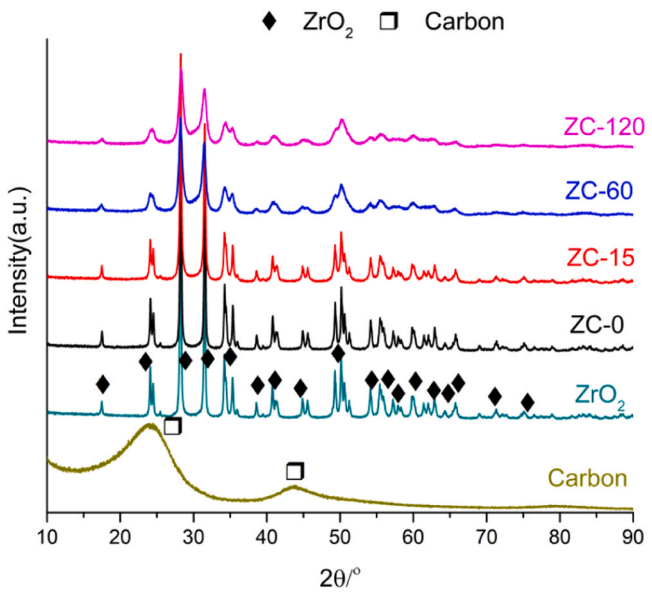

Fig. 1. XRD patterns of the starting powders and mechanically activated mixtures.

Table 1
Phase identification, crystallite size, and strain for the starting powders and the mechanically activated mixtures.

Sample	Phases	Crystallite size (Å)	Strain (%)
ZrO_2	ZrO_2	398(23)	0.10(3)
C			
ZC–0	ZrO_2	391(18)	0.09(3)
	C	53.0(3)	0.85(7)
ZC–15	ZrO_2	284(39)	0.17(1)
	C	34.4(12)	4.4(3)
ZC–60	ZrO_2	132(19)	0.76(14)
	C	26.88(6)	1.41(8)
ZC–120	ZrO_2	79(4)	0.2(4)
	C	25.09(6)	1.20(1)

aids. Another alternative, prior to sintering, is mechanical activation (MA), which is a high-energy ball milling process that induces physicochemical changes in the starting ceramic particles [22,23]. MA reduces particle size and produces defects in materials which increase the chemical activity, promote densifying sintering mechanisms, increase the rate of densification, and, therefore, decrease the sintering time and temperature. MA leads to formation of the defects such as grain boundaries, strain and dislocations, as well as lattice defects [24]. The most common lattice defects produced during MA are oxygen vacancies, cation interstitials, cationic vacancies and oxygen interstitials [25]. Furthermore, mechanical activation can also affect the final physical properties of sintered bodies. Hence, milling processes are low-cost attractive methods because they enable the formation of submicron and/or nano-structured materials with desirable properties [26–31].

In this paper, we studied the influence of mechanical activation of ZrO_2-C powder mixtures on carbothermal reduction, phase composition, microstructure, densification, and mechanical properties of sintered ZrC ceramics.

2. Experimental procedure

A mixture of high-purity ZrO_2 (99.9% purity Sigma–Aldrich, p.a.) and carbon black (C, BP1100, Cabot) starting powders were used in these experiments. The starting ZrO_2 and C were mixed in ratio corresponding to the expected reaction:

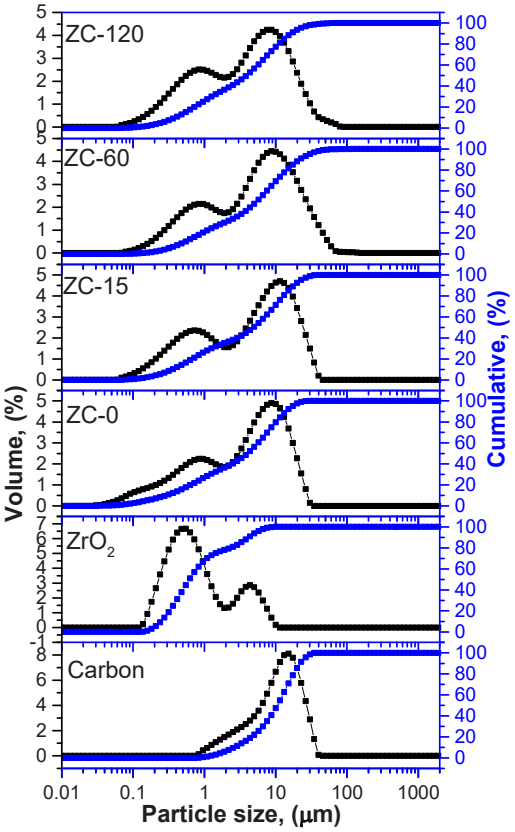

Fig. 2. Particle size distribution of the C, ZrO_2 and ZC mixtures, measured by DLS.

Table 2
Characteristic values of d(0.1), d(0.5), d(0.9) and *span* for C, ZrO_2 and powder mixtures.

Sample	d (0.1) μm	d (0.5) μm	d (0.9) μm	Span (μm)
Carbon	2.619	10.526	22.105	1.851
ZrO_2	0.247	0.619	4.165	6.334
ZC–0	0.292	4.018	13.876	3.381
ZC–15	0.354	4.872	17.970	3.615
ZC–60	0.476	5.410	21.812	3.944
ZC–120	0.392	3.898	16.368	4.099

$$ZrO_2 + 3\,C = ZrC + 2CO\uparrow \quad (1)$$

The powder mixture was mechanically activated for 15, 60, and 120 min in a high-energy planetary ball mill (Planetary Ball Mill Retsch PM 100) in air. MA was performed by using Y-stabilized ZrO_2 vials and balls. The milling balls were 5 mm in diameter and the jar volume was 500 ml. The ball-to-powder weight ratio was 40:1 with a rotation speed of 400 rpm. Individual MA runs were done with 15 g of the powder mixture and 600 g of the ZrO_2 media. Milling times of 15 min and 60 min were conducted in a single step while the 120 min milling time was conducted in two 60 min steps with a 30 min cooling period between steps. Powders were sieved after milling to remove any large debris. The powder mixtures were labelled based on the activation time as ZC–0 for no milling up to ZC–120 for 120 min of milling. The use of zirconia balls and media minimizes the introduction of impurities from milling since zirconia is one of the reactants used in the synthesis reaction.

Milled powders were characterized at room temperature by X-ray powder diffraction (XRPD) method using Ultima IV Rigaku diffractometer, equipped with $CuK\alpha_{1,2}$ radiation, using a voltage of 40.0 kV and current of 40.0 mA. The samples were placed on a Si-monocrystalline sample carrier. The range of 10–80° 2θ was used for all powders in a

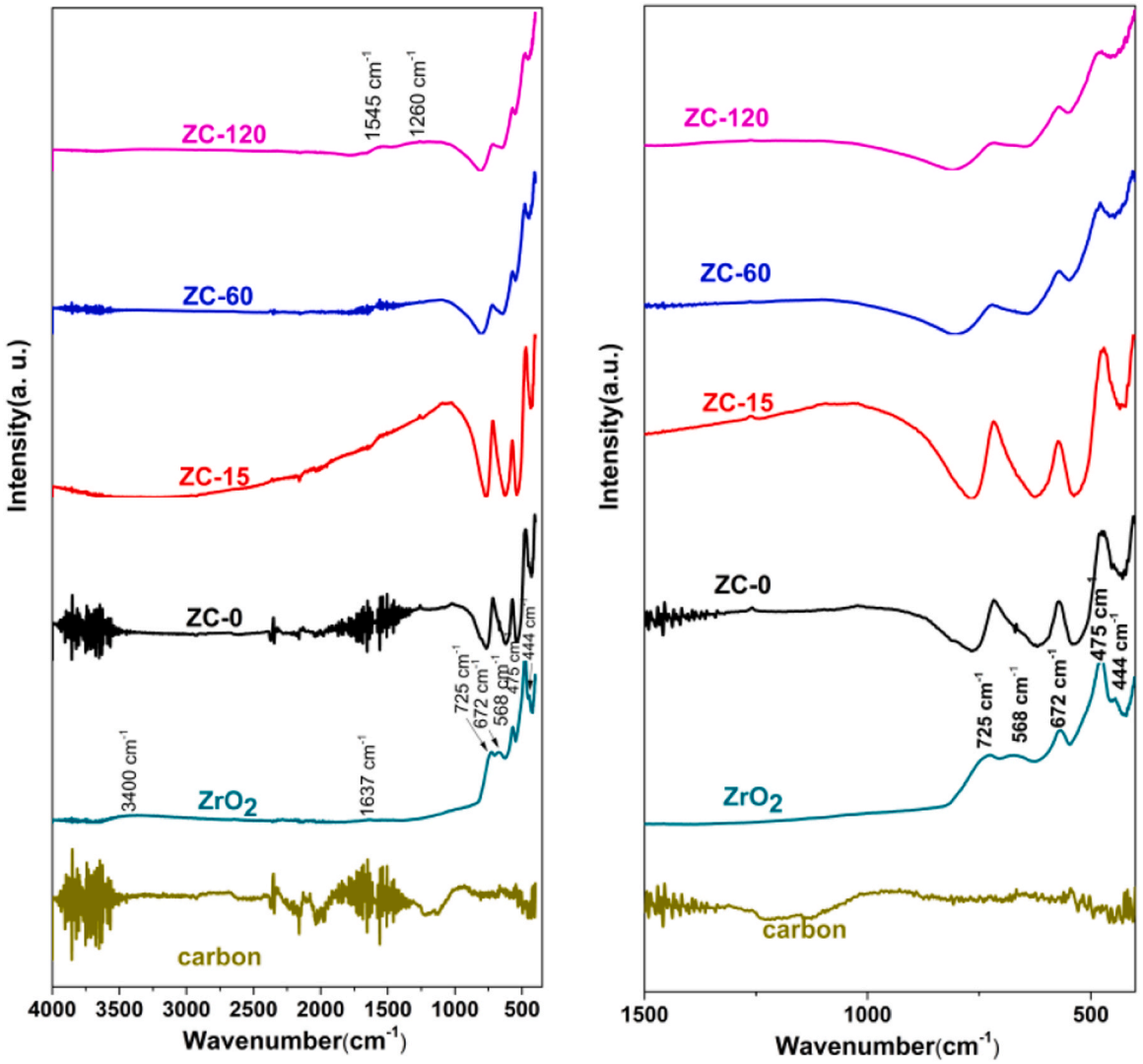

Fig. 3. ATR-FTIR spectra of the commercial powders and mechanically activated mixtures. Note that the panel on the right is an expansion of the range between 1500 cm^{-1} and 400 cm^{-1} from the full spectra on the left panel.

Table 3
SSA of powders after milling and after carbothermal reaction.

Sample	After milling (m^2/g)	After reaction (m^2/g)
ZC–0	60.8	4.2
ZC–15	63.6	4.4
ZC–60	83.0	4.1
ZC–120	62.0	4.8

continuous scan mode with a scanning step size of 0.02° and at a scan rate of 5 °/min, using D/TeX Ultra high - speed detector. Powder diffraction file (PDF) card numbers that were used for phase identification were: 01–083–0940 for monoclinic ZrO_2, 01–089–8493 for C, and 03–065–0973 for ZrC. Crystallite size and strain were estimated from peak broadening by Rietveld refinement. The particle size distributions were investigated by the laser diffraction on Mastersizer 2000 Malvern Instruments Ltd., where powders were dispersed in isopropanol. The instrument covers the particle size range of 0.02–2000 μm. Prior to measurements, the powders were subjected to low power ultrasound treatment for 5 min. Fourier-transform infrared (FTIR) spectroscopy spectra were collected using FTIR Nicolet 6700 ATR device (Thermo Fisher, UK), in spectral range 400–4000 cm^{-1}. The instrument resolution was 4 cm^{-1}. The spectra were measured in air at room temperature. The

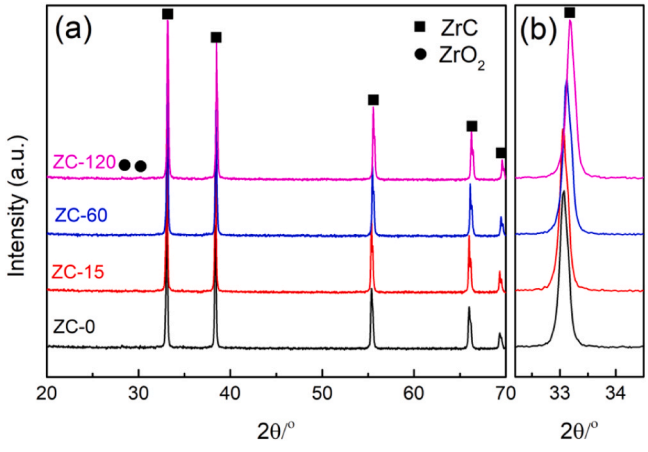

Fig. 4. XRD of reacted powders.

specific surface area (SSA) of mechanically activated powders and powders after carbo-thermal reaction was determined by nitrogen absorption (NOVA 1000, Quantachrome, Boynton Beach, FL, USA) and

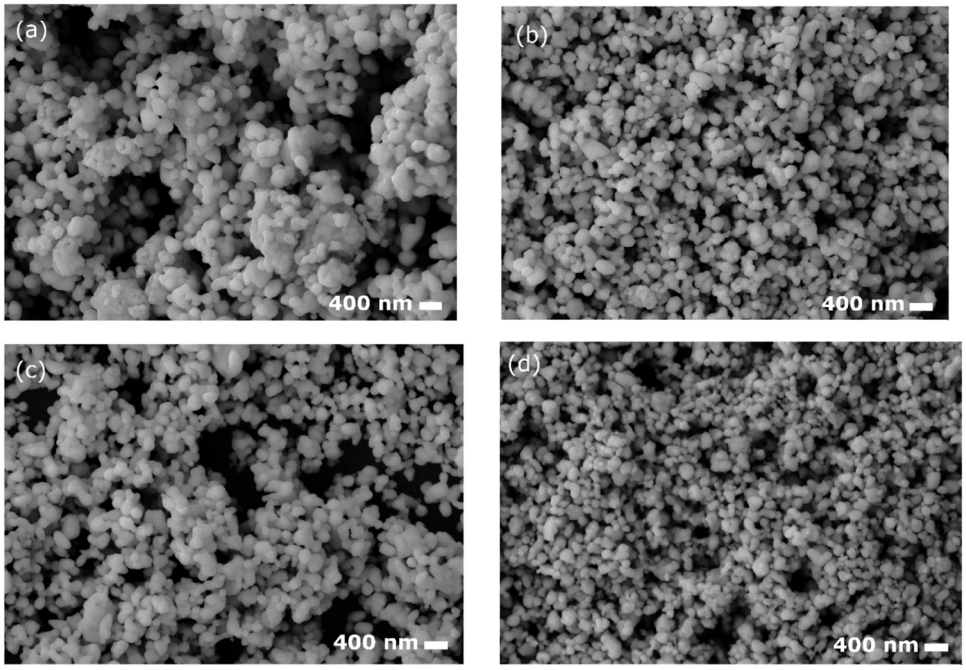

Fig. 5. SEM micrographs of reacted powders: a) ZC–0, b) ZC–15, c) ZC–60, and d) ZC–120.

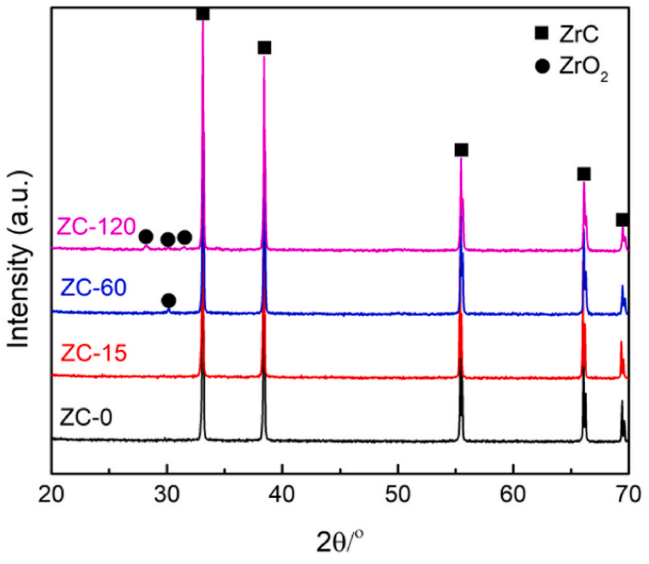

Fig. 6. XRD patterns of SPS specimens.

BET analysis.

Powders were reacted in a graphite crucible. The thermal treatment cycle included heating at 10 °C/min to 1600 °C followed by an isothermal hold for 2 h hold in vacuum (~20 Pa) in a resistance-heated graphite element furnace (HP50–7010 G, Thermal Technology, Santa Rosa, CA). This first step of the process promoted carbothermal reaction of the starting materials. The resulting ZrC powder was densified by SPS in graphite dies. The peak densification temperature was 2000 °C with an isothermal holding time of 10 min. The heating rate of SPS was 15 °C/min with an isothermal hold at 1600 °C and applied pressure of 15 MPa for 5 min. The applied pressure during densification was 50 MPa. Based on the use of the stoichiometric amount of carbon for Reaction 1 and the use of a graphite crucible for reaction and graphite die for densification, the carbon contents of the final ZrC ceramics were assumed to be close to stoichiometric and consistent among the four different specimens.

Bulk density was measured using a modified Archimedes' method with distilled water as the immersion liquid (ASTM C373). Powder X-ray diffraction (XRD) patterns were collected from portions of samples which had been crushed with a zirconia mortar and pestle and sieved to 200 mesh. (X'Pert Pro, PANalytical, Almelo, Netherlands) Diffraction patterns were collected between 20 and 70 ° 2θ, with a step size of 0.026 ° 2θ, and an effective time per step that resulted in a total scan time of 30 min. The diffractometer was set to use a tube current of 40 mA, a generator voltage of 45 keV, and Cu-Kα radiation (λ = 1.54056 Å). The PDXL2 (Ver. 2.8.4.0) software was used for phase analysis [32]. All obtained phases were identified using the ICDD data base [33]. RIQAS Rietveld refinement software was used to analyze sample lattice parameters. Specimens were prepared for scanning electron microscopy (SEM) by surface grinding reaction layers from billet surfaces and polishing with progressively finer diamond polishing pads and diamond slurries to a final surface finish of 0.25 μm. Imaging was performed with an accelerating voltage of 5 kV, a working distance of 10 μm, and an aperture of 15 μm to enhance channelling contrast to distinguish individual grains (e-Line Plus, RAITH, Dortmund, Germany). Energy dispersive spectrometry (EDS) was performed with an accelerating voltage of 15 kV at a working distance of 5.1 mm, and an emission current of 1.4 nA (Helios NanoLab DualBeam 600, Thermo Fisher Scientific, Waltham, MA; AZtec, Oxford Instruments, Abingdon, United Kingdom). The microscope was equipped with a Si(Li) detector with an area of 50 mm^2. Maps were acquired with a resolution of 1024 × 800 px at a dwell time of 150 μs over 1 frame. Grain sizes were determined by analyzing > 400 grains using image processing software to calculate their Feret diameter (ImageJ, National Institutes of Health, Bethesda, MD).

Vickers hardness testing was performed on polished portions of samples prepared in the manner described above for SEM analysis. Indentations were performed according to ASTM C1327 with an applied load of 9.81 N for 10 s (Duramin 5, Leco, St. Joseph, MI). A minimum of 24 indents were measured for each specimen to calculate the reported averages and standard deviations.

3. Results and discussion

XRD analysis shown in Fig. 1 and summarized in Table 1 revealed

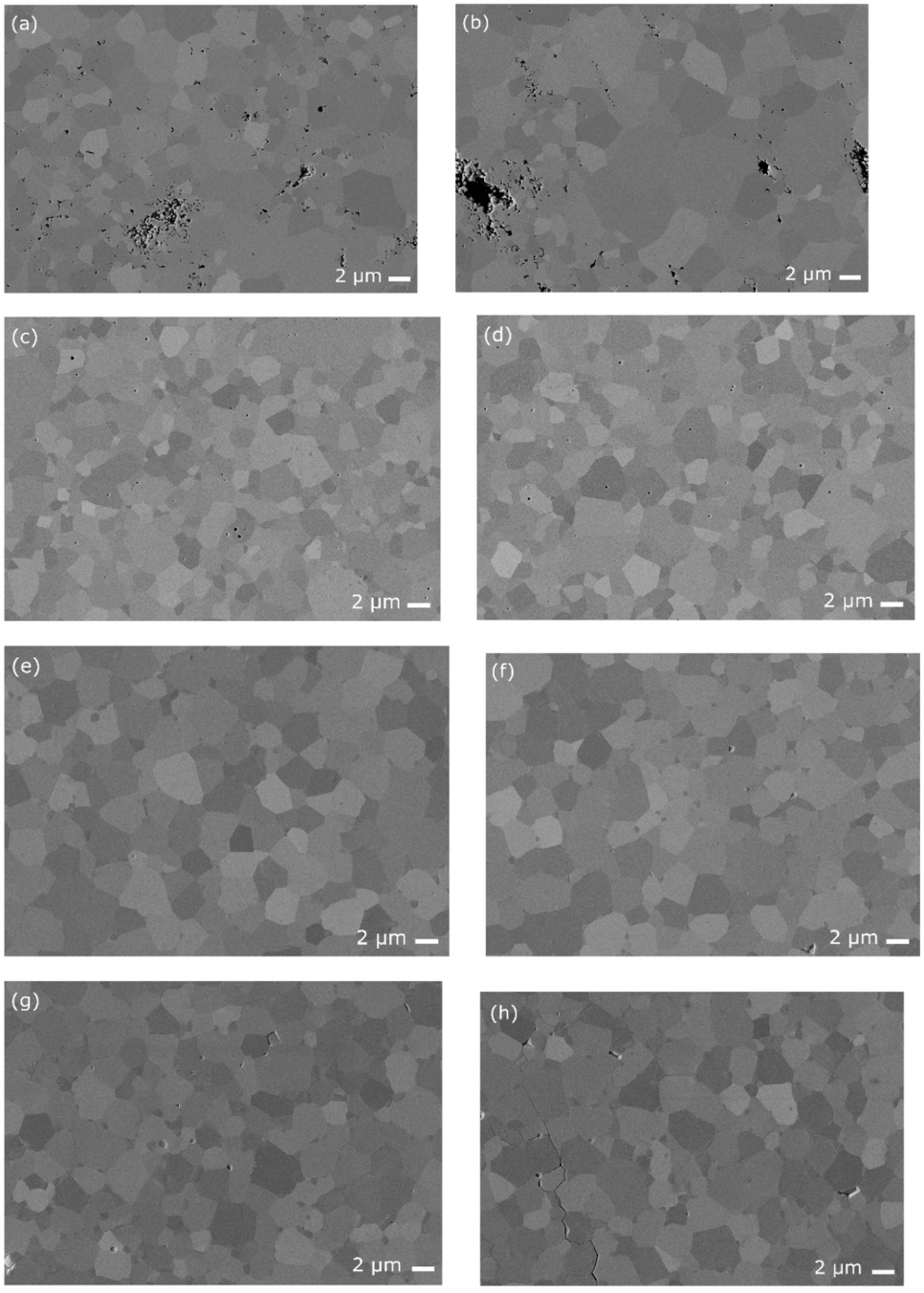

Fig. 7. SEM micrographs of SPS specimens: a, b) ZC–0, c, d) ZC–15, e, f) ZC–60, and g, h) ZC–120.

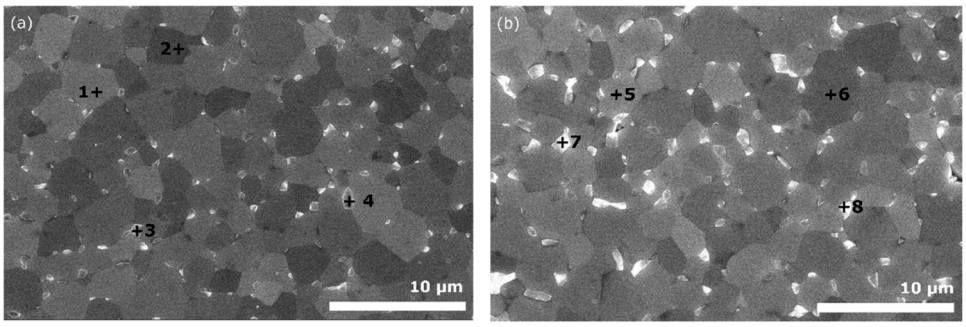

Fig. 8. SEM micrographs of a) ZC–60, and b) ZC–120 showing the points for EDS analysis listed in Table 4. The lighter colored regions such as points 3, 4, 7, and 8 are ZrO_2 and the darker grains are ZrC.

Table 4
Results of EDS analysis.

Sample	Points	Elements (at%)		
		Zr	C	O
ZC–60	1	55.53	42.11	4.36
	2	55.59	40.81	3.60
	3	39.51	21.65	38.84
	4	38.01	20.02	41.98
ZC–120	5	46.08	49.73	4.2
	6	47.19	49.06	3.75
	7	33.03	27.46	39.51
	8	31.02	25.62	43.36

that the starting ZrO_2 was highly crystalline with low level of structural strain, around 0.1%. According to structural data it is monoclinic symmetry, with space group P121/c1. On the other hand, the diffraction pattern of the C suggests that it is amorphous with higher strain as indicated by peak shifts from the positions listed on the PDF cards. The diffraction peaks were sharp and intense for the starting ZrO_2 powder and for ZrO_2 in the mixtures denoted as ZC–0 and ZC–15, indicating well-ordered crystalline phases. With the increase of milling period (60 min and higher), the peaks for ZrO_2 broadened, indicating a decrease in crystallite size and an increase of the structural strain.

The results of particle size analysis are presented in Fig. 2 with average particle size, d(0.5) along with the tenth percentile, d(0.1) and ninetieth percentile d(0.9) also reported. The particle size of the commercial carbon powder showed a bimodal distribution with the dominant volume fraction of the particles having a diameter of about 10 μm. A smaller, but notable volume of particles had diameters below 5 μm. Laser diffraction cannot distinguish agglomerates from single particles, which is likely the reason for the larger particles that were observed. The ZrO_2 powder is significantly finer, with the major particles fraction around 0.6 μm in diameter with a secondary concentration of about 4 μm in diameter, which probably indicates agglomerates. Mechanically activated powders show poly-modal distribution with characteristic parameters present in Table 2. In general, increasing milling time appears to increase the fraction of particles in the lower size range, but does not change d(0.1) or d(0.5) significantly. The span values that depict the width of the distribution (in μm) are also given in the Table 2.

The FTIR spectra are given in Fig. 3. The spectrum of the commercial ZrO_2 shows peaks at 444 cm^{-1}, 475 cm^{-1}, 568 cm^{-1}, 672 cm^{-1}, 725 cm^{-1}, a small intensity peak at 1637 cm^{-1}, and a broad peak at 3400 cm^{-1}. The first band is related to Zr–O–Zr vibrations [34]. Second set of peaks between 450 and 800 cm^{-1} originate from vibrations of Zr–O [35]. The peak at 725 cm^{-1} is assigned to ZrO^{4+} tetrahedral vibration modes. The small intensity vibration band at 1637 cm^{-1} is correlated with the bending mode of adsorbed water [34–36]. The surface of zirconia is known to be covered by hydroxyl groups that coordinate to single Zr ions (terminal –OH groups) or multi-coordinated –OH groups (–OH coordinated to two or three Zr ions) [35]. Amorphous structure of carbon, observed XRD as broad peaks, was confirmed by FTIR. The vibration modes expected for well-ordered crystalline graphite are missing. In the spectrum of the ZC–0 sample, all of the modes detected in the starting powders were present. With increasing milling time, the peaks at 444 cm^{-1} and 725 cm^{-1} disappear due to breaking of some bonds during particle comminution. Also, the widening of modes and changes in their shapes are likely to be the consequence of defects introduced into the structure that change the lattice vibrations. The broadening of the vibration modes is consistent with the changes in strain noted in the XRD data and changes in SSA discussed below.

Two new vibration modes were detected in ZC–60 and ZC–120 at 1260 cm^{-1} and 1545 cm^{-1}. These peaks can be ascribed to C–O and C═C vibrations, respectively [37,38]. The mode of ZrC located at ~1383 cm^{-1} wasn't detected in spectra of ZC–60 and ZC–120, which indicates that carbothermal reduction was not promoted by milling. In samples subjected to longer mechanical treatment presence of modes originating from O–H stretching vibrations disappear, owing to removal of adsorbed water molecules when powder heating occurred during milling.

The results of SSA measurements are summarized in Table 3. Specific surface area of ZC–0 powder was around 60 m^2/g. As milling time increased, surface area of powders increased, showing its maximum of 83 m^2/g for sample ZC–60, indicating particle size reduction. The values are high due to high SSA of C that dominates the results. The decrease in surface area from 83 m^2/g for sample ZC–60–62 m^2/g for ZC-120 is likely due to re-welding of the particles due to the longer milling time, which is consistent with the decrease in strain shown for these powders in Table 1. After carbothermal reaction, SSA was significantly lower, around 4 m^2/g in all powders. The lower surface area indicated that most or all of the carbon reacted. In addition, the mean particle diameter estimated from the surface area was about 81 nm for the synthesized ZrC assuming spherical particles and a true density of 6.73 g/cm^3 for ZrC.

After reaction, all four XRD patterns showed that pure ZrC was present with sharp and intense peaks as shown in Fig. 4. The most intense ZrC peak at around 33° 2θ was shifted to higher angles for powders prepared with longer milling times (enlarged peaks shown in Fig. 4b.). This shift could be due to higher carbon content or a higher concentration of dissolved oxygen in the resulting ZrC [2]. The decrease in lattice parameter (from 0.4690 nm for ZC–0–0.4676 nm for ZC–120) was confirmed by Rietveld refinement.

Scanning electron micrographs of the reacted powders are presented in Fig. 5. SEM micrograph of ZC–0 shows round spherical particles that

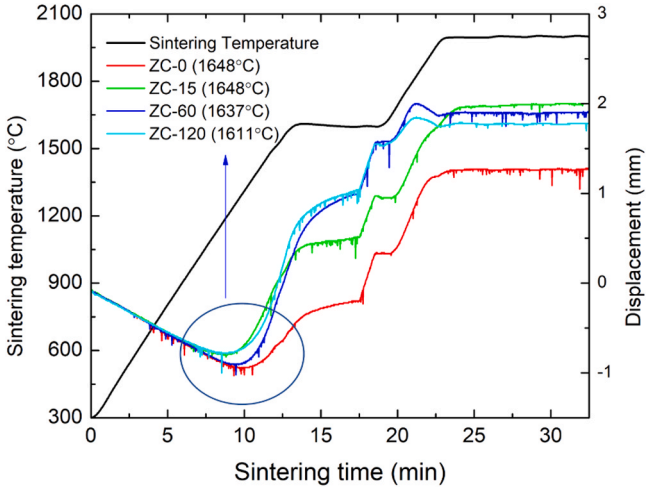

Fig. A1. Sintering curves of samples ZC–0, ZC–15, ZC–60, and ZC–120.

Table 5
Bulk densities, grain size, hardness, and onset of densification temperature of SPS specimens.

Sample	Bulk ρ (g/cm^3)	Relative ρ (%)	Grain Size surface (μm)	Grain Size cross-section (μm)	Hardness (GPa)	Densification Onset (°C)
ZC–0	6.66	~98	2.4 ± 1.4	2.7 ± 2.2	15.8 ± 0.8	1648
ZC–15	6.77	~100	1.9 ± 0.9	2.0 ± 1.0	16.4 ± 0.4	1648
ZC–60	6.76	~100	2.9 ± 1.0	2.8 ± 1.0	16.8 ± 1.0	1637
ZC–120	6.75	~100	2.3 ± 1.1	2.5 ± 1.2	15.9 ± 1.1	1611

were agglomerated into larger, multi-particle aggregates. As the time of mechanical activation increased, the size of the primary particles decreased, and the particles appeared to be less agglomerated. Particle sizes determined from image analysis confirmed the decrease in size with increasing mechanical activation time, from 236 ± 71 nm for ZC–0–146 ± 49 nm for ZC–120.

After SPS, nominally phase-pure ZrC was present in ZC–0 and ZC–15, with well-defined, sharp and intense peaks. No peaks for ZrO_2 were noted in ZC–0 or ZC–15. However, some ZrO_2 was detected after reaction in samples activated for 60 and 120 min. With the increase of milling time, the ZrO_2 content of the reacted powders increased, indicating that the powders were deficient in carbon during reaction. The carbon deficiency could be caused by either oxidation of some C during milling or incorporation of additional ZrO_2 due to wear of media during milling. The smaller particle size induced by longer milling times also increases the surface area of the reacted powders, which could lead to increased formation of native oxide on the reacted powders, which could lead to higher oxygen contents with increased milling time. Fig. 6.

Microstructures of the polished surfaces and cross-sections of the dense ZrC ceramics are shown in Fig. 7. ZC–0 is characterized by grains that vary in size and shape, from 1.5 to 5 μm. The specimen also contains some small black areas with circular cross section that are residual carbon and larger black areas that are porosity. These flaws are apparent in both the surface and cross section images. The flaws are typically clustered in areas larger than ~2 μm and are presumably caused by poor homogenization of the starting powders (i.e., agglomeration of the starting ZrO_2, carbon, or both). The average grain size for non-milled specimen on the surface was 2.4 ± 1.4 μm, and on the cross-section 2.7 ± 2.2 μm. The similar grain sizes on the surface and cross section views indicate that grain size was uniform throughout the dense billet. In addition, the two views are perpendicular, which demonstrates that no significant grain texturing was induced by SPS. Specimen ZC–15 had much smaller grains that were equiaxed and less than 2 μm in diameter, with no porosity. Similar to ZC-0, grain sizes were similar on the surface and in cross section indicating uniform grain size and lack of any significant microstructural texturing. Longer milling times of 60 or 120 min prior to thermal treatment led to larger grains (2.9 ± 1.0 μm for ZC–60 and 2.3 ± 1.1 μm for ZC–120) and the presence of impurities in the final ceramics. The larger grain size of ZC-60 likely indicates a higher densification rate for the longer milling time while the decrease for ZC-120 may be due to the higher level of ZrO_2 impurities in the final ceramic.

Fig. 8. is shows SEM micrographs of the final ceramics that contained significant amounts of milling-induced ZrO_2 impurities, ZC-60 and ZC-120, with labels indicating points where EDS analysis was performed. White dots represent the locations where oxygen impurities were concentrated in the specimens, presumably as crystalline ZrO_2 that detected by XRD for these compositions. The amounts of the ZrO_2 impurities calculated by image analysis were 4.2 vol% in ZC-60 and 8.3 vol % in ZC-120. Table 4 summarizes the compositions at the points shown in Fig. 8. Dots 3, 4, and 7, 8 are rich in oxygen, which indicates that prolonged mechanical activation times led to the presence of impurities on the grain boundaries.

Bulk densities after SPS, grain size, and Vickers hardness are presented in Table 5. The non-activated sintered specimen, ZC–0 had a bulk density of 6.66 g/cm^3 and hardness of 15.8 GPa. ZC–0 did not reach full density and the onset sintering temperature was 1648 °C (see Fig. A1.). All of the materials that were mechanically activated prior to sintering exhibited higher values of relative density. Mechanical activation also shifted the onset of densification to lower temperatures reaching as low as 1611 °C for ZC–120. In addition, all of the ceramics prepared from powders that were mechanically activated reached nearly full density. The best combination of properties was for ZC–15, which exhibited ~100% TD with the highest hardness of 16.4 ± 0.4 GPa. The presence of ZrO_2 in ZC-60 C and ZC-120 C does not alter the hardness significantly since zirconia typically has a hardness of about 15 GPa, which is similar to the ZrC matrix [39].

4. Conclusions

Based on the results presented in this paper, the conclusions that can be drawn are:

- ZrC ceramics with high relative density were produced by carbothermal reduction synthesis and densified by SPS;
- Mechanical activation leads to decreases in the particle size and increases in the SSA from about 60 m^2/g for ZC-0 to as high as ~80 m^2/g for ZC-60. The decreased particle size and increased surface area of the powders more reactive and decreases the onset temperature for densification by as much as much as ~40 °C;
- Based on densification data and impurity levels, a milling time of 15 min appears to give the best balance of particle size reduction to promote densification while minimizing impurity level.

Declaration of Competing Interest

The authors have no conflict of interest related to this paper.

Acknowledgement

This work was supported by the Ministry of Science, Technological Development and Innovation of the Republic of Serbia (Contract No. 451-03-47/2023-01/200175, 451-03-47/2023-01/200135, and 451-03-47/2023-01/ 200017) and the NATO Science for Peace and Security Programme under grant MYP-G5767 (SUSPENCE).

Appendix

see Appendix Fig. A1

References

[1] B. Nayebi, N. Parvin, M.S. Asl, Role of carbon morphology on the synthesizability of ZrC during spark plasma sintering of ZrB_2-Z-C composites, J Taiwan Instit. Chem. Eng. 117 (2020) 252–256.
[2] H.F. Jackson, W.E. Lee, Properties and characteristics of ZrC, in: R.J.M. Konings (Ed.), in Comprehensive Nuclear Materials, vol. 2, Elsevier, Amsterdam, Netherland, 2012, pp. 339–372.
[3] S. Wang, M. Liu, X. Liu, Q. Jia, S. Zhang, Carbothermal reduction synthesis of high porosity and low thermal conductivity ZrC-SiC ceramics via an one-step sintering technique, J. Eur. Ceram. Soc. 42 (2022) 4465–4471.
[4] Y. Katoh, G. Vasudevamurthy, T. Nozawa, L.L. Snead, Properties of zirconium carbide for nuclear fuel applications, J. Nuc. Mater. 441 (2013) 718–742.
[5] A.A. Mahday, M.S. EI-Eskandarany, H.A. Ahmed, A.A. Amer, Mechanically induced solid state carburization for fabrication of nanocrystalline ZrC refractory material powders, J. Alloy. Compd. 299 (2000) 244–253.
[6] T. Tsuchida, M. Kawaguchi, K. Kodaira, Synthesis of ZrC and ZrN in air from mechanically activated ZrC and powder mixtures, Solid State Ion. 102–103 (1997) 149–154.
[7] A. Maitre, P. Lefort, Solid state reaction of zirconia with carbon, Solid State Ion. 104 (1997) 109–122.
[8] M.D. Sacks, C.A. Wang, Z.H. Yang, A. Jain, Carbothermal reduction synthesis of nanocrystalline zirconium carbide and hafnium carbide powders using solution-derived precursors, J. Mater. Sci. 39 (2004) 6057–6066.
[9] J.J. Xie, Z.Y. Fu, Y.C. Wang, S.W. Lee, K. Niihara, Synthesis of nanosized zirconium carbide powders by a combinational method of sol-gel and pulse current heating, J. Eur. Ceram. Soc. 34 (13) (2014) e1–13.e7.
[10] M.N. Seo, S.H. Kang, Y.M. Kim, S.S. Ryu, Preparation of highly dispersed ultra-fine ZrC by combination of carbothermal reduction of ball-milled ZrO_2 and C mixture and bead milling, Int. J. Refract. Met. Hard Mater. 41 (2013) 345–350.
[11] Y.J. Yan, Z.R. Huang, X.J. Liu, D.L. Jiang, Carbothermal synthesis of ultra-fine zirconium carbide powders using inorganic precursors via sol-gel method, J. Sol. Gel Sci. Technol. 44 (2007) 81–85.
[12] K. Schönfeld, H.P. Martin, A. Michaelis, Pressureless sintering of ZrC with variable stoichiometry, J. Adv. Ceram. 6 (2) (2017) 165–175.
[13] C. Ang, T. Williams, A. Seeber, H.T. Wang, Y.B. Cheng, Synthesis and evolution of zirconium carbide via sol-gel route: features of nanoparticle oxide-carbon reactions, J. Am. Ceram. Soc. 96 (2013) 1099–1106.
[14] L. Feng, W.G. Fahrenholtz, G.E. Hilmas, Low-temperature sintering of single-phase, high-entropy carbide ceramics, J. Am. Ceram. Soc. 102 (2019) 7217–7224.

[15] L. Feng, S. Lee, H. Lee, Nano-sized zirconium carbide powder: synthesis and densification using a spark plasma sintering apparatus, Int. J. Refract. Met. Hard Mater. 64 (2017) 98–105.
[16] Z.A. Munir, D.V. Quach, M. Ohyanagi, Electric current activation of sintering: review of the pulse electric current sintering process, J. Am. Ceram. Soc. 94 (2011) 1–19.
[17] N. Korklan, G.E. Hilmas, W.G. Fahrenholtz, Processing and room temperature mechanical properties of a zirconium carbide ceramic, J. Am. Ceram. Soc. 104 (2021) 413–418.
[18] L. Feng, W.G. Fahrenholtz, G.E. Hilmas, Y. Zhou, Synthesis of single-phase high-entropy carbide powders, Scr. Mater. 162 (2019) 90–93.
[19] Y. Tian, W. Sun, Synthesis of ZrB_2–ZrC hybrid powders via boro-carbothermal reduction of ZrO_2 by B_4C and carbon black, Ceram. Inter 48 (2022) 26499–26507.
[20] H. Chen, F. Zeng, W. Li, J. Liu, Y. Gu, F. Zhang, Densification behaviour and mechanical properties of spark plasma reaction sintered ZrB_2–ZrC-B_4C ceramics from B_4C-Zr system, Ceram. Inter 45 (2019) 12122–12129.
[21] N. Obradovic, W.G. Fahrenholtz, C. Corlett, S. Filipovic, M. Nikolic, B. A. Marinkovic, S. Failla, D. Sciti, D. Di Rosa, E. Sani, Microstructural and optical properties of $MgAl_2O_4$ Spinel: effects of mechanical activation, Y_2O_3 and graphene additions, Materials 14 (2021) 7674.
[22] M.S. Abdi, T. Ebadzadeh, A. Ghaffari, M. Feli, Synthesis of nano-sized spinel ($MgAl_2O_4$) from short mechanochemically activated chloride precursors and its sintering behaviour, Adv. Powd. Technol. 26 (2015) 175–179.
[23] N. Obradović, W.G. Fahrenholtz, S. Filipović, C. Corlett, P. Đorđević, J. Rogan, P. J. Vulić, V. Buljak, V. Pavlović, Characterization of $MgAl_2O_4$ sintered ceramics, Sci. Sinter. 51 (2019) 363–376.
[24] M. Zakeri, M.R. Rahimipour, B.J. Abbasi, Synthesis of nanostructure tetragonal ZrO_2 by high energy ball milling, Mater. Technol. 28 (4) (2013) 181–186.
[25] C.A. Aggelopoulos, M. Dimitropoulos, A. Govatsi, L. Sygellou, C.D. Tsakiroglou, S. N. Yannopoulos, Influence of the surface-to-bulk defects ratio of ZnO and TiO_2 on their UV-mediated photocatalytic activity, Appl. Cat. B Environ. 205 (2017) 292–301.
[26] J. Li, M. Hitch, Economic analysis on the application of mechanical activation in an integrated mineral carbonation process, Inter. Biodeter. Biodegrad. 128 (2018) 63–71.
[27] A. Peleš, N. Đorđević, N. Obradović, N. Tadić, V.B. Pavlović, Influence of prolonged sintering time on density and electrical properties of isothermally sintered cordierite-based ceramics, Sci. Sinter. 45 (2013) 157–164.
[28] S. Filipović, N. Obradović, V.B. Pavlović, M. Mitrić, A. Đorđević, M. Kachlik, K. Maca, Effect of consolidation parameters on structural, microstructural and electrical properties of magnesium titanate ceramics, Ceram. Int. 42 (2016) 9887–9898.
[29] D. Kosanović, N.J. Labus, J. Živojinović, A. Peles Tadić, V.A. Blagojević, V. B. Pavlović, Effects of mechanical activation on the formation and sintering kinetics of barium strontium titanate ceramics, Sci. Sinter. 52 (2020) 371–385.
[30] C.A. Corlett, M.D. Frontzek, N. Obradovic, J.L. Watts, W.G. Fahrenholtz, Mechanical activation and cation site disorder in $MgAl_2O_4$, Materials 15 (2022) 6422.
[31] J. Živojinović, D. Kosanović, V.A. Blagojević, V.P. Pavlović, N. Tadić, B. Vlahović, V.B. Pavlović, Dielectric properties of mechanically activated strontium titanate ceramics, Sci. Sint. 54 (2022) 401–414.
[32] P.D.X.L. Rigaku, Integrated X-Ray Powder Diffraction Software, Rigaku,, Tokyo: Japan, 2011.
[33] International Crystallographical Database (ICDD). PDF-2 Release 2012; ICDD: Newtown Square, PA, USA, (2012).
[34] Y. Adraider, Y.X. Pang, F. Nabhani, S.N. Hodgson, M.C. Sharp, A. Al-Waidh, Fabrication of zirconium oxide coatings on stainless steel by a combined laser/sol–gel technique, Ceram. Inter 39 (2013) 9665–9670.
[35] N.Y. Mostafa, M.M. Qhtani, S.H. Alotaibi, Z.I. Zaki, S. Alharthi, M. Cieslik, K. Gornicka, J. Ryl, R. Boukherroub, M.A. Amin, Cathodic activation of synthesized highly defective monoclinic hydroxyl-functionalized ZrO_2 nanoparticles for efficient electrochemical production of hydrogen in alkaline media, Int. J. Energy Res. (2020) 1–15.
[36] M. Catauro, F. Barrino, M. Bononi, E. Colombini, R. Giovanardi, P. Veronesi, E. Tranquillo, Coating of titanium substrates with ZrO_2 and ZrO_2-SiO_2 composites by Sol-Gel synthesis for biomedical applications: structural characterization, mechanical and corrosive behavior, Coatings 9 (2019) 200.
[37] Y. Li, S. Chen, H. Hu, C. Zou, Z. Chen, X. Ma, A meltable precursor for zirconium carbide ceramics and C/C-ZrC composites, Ceram. Inter 44 (9) (2018) 10175–10180.
[38] N. Patra, D.D. Jayaseelan, W.E. Lee, Synthesis of biopolymer-derived zirconium carbide powder by facile one-pot reaction, J. Am. Ceram. Soc. 98 (1) (2015) 71–77.
[39] R.A. Cutler, R.J. Mayhew, K.M. Prettyman, A. Virkar, High-Toughness Ce-TZP/Al_2O_3 ceramics with improved hardness and strength, J. Am. Ceram. Soc. 74 (1) (1991) 179–186.